



Solvent-mediated oxidative polymerization to atomically dispersed iron sites for oxygen reduction

Xiuyun Yao^a, Youqi Zhu^{a,*}, Zhanli Han^a, Lifan Yang^a, Jiachen Tian^a, Tianyu Xia^b, Hui Peng^c, Chuanbao Cao^{a,*}

^a Research Center of Materials Science, Beijing Key Laboratory of Construction Tailorable Advanced Functional Materials and Green Applications, Beijing Institute of Technology, Beijing 100081, China

^b Key Laboratory of Material Physics Ministry of Education, School of Physics and Microelectronics, Zhengzhou University, Zhengzhou 450052, China

^c Analysis and Testing Center, Shandong University of Technology, Zibo 255000, China

ARTICLE INFO

Keywords:

Fe single-atom catalyst
Chemical state evolution
High open circuit potential
Ultra-long cycling stability
Alkaline reversible Zn-air batteries

ABSTRACT

Fe single-atom catalysts open up broad prospects for oxygen reduction reaction (ORR), but the chemical state evolution of Fe species before forming isolated sites is rarely understood. Herein, mechanistic investigation on the formation of isolated Fe sites is presented through solvent-mediated oxidative pyrrole polymerization strategy. The slow reaction kinetics of oxidative Fe³⁺ ions with the predesigned methanol solvent molecules can endow highly dispersed Fe sites in polypyrrole and thus Fe single-atom catalysts after pyrolysis. The Fe single-atom catalyst (Fe-SA/PNC) performs superior ORR activity with a half-wave potential of 0.90 V versus RHE and 12.8 times higher turnover frequency than that of commercial Pt/C. When assembled into Zn-air batteries, the Fe-SA/PNC cathode delivers a 1.68 V open circuit potential and ultra-long cycling stability over 9000 cycles, superior to the most reported catalysts so far. Experimental and theoretical results reveal that the rich adjacent non-coordinated graphitic nitrogen atoms can enhance electronic conductivity and promote O₂ adsorption and OH⁻ desorption, thus enabling high oxygen reduction and battery performances.

1. Introduction

The electrochemical oxygen reduction plays a crucial role in the emerging energy-related technologies including fuel cells and metal-air batteries, but suffers from sluggish kinetics and insufficient operation durability over various practical catalysts [1–4]. While platinum group metal catalysts have been well exploited and shown high activities, their high cost, scarcity and low stability severely restrict their viability of sustainable development [5–7]. Therefore, developing high-efficiency and durable non-precious metal alternatives is highly required yet still challenging. Recently, transition metal single-atom catalysts have attracted great attentions due to nearly 100% atom utilization, high activity, and durability [8–16]. Practically, the well-defined local atomic structure can be precisely designed on single-atom catalysts to generate abundant porosity, high surface area and mostly exposed active sites accessible to reactants [7,11,17,18]. Significant efforts have been devoted to developing a variety of synthetic strategies to construct efficient single-atom catalysts [19–22]. However, protecting atomically dispersed metal active centers from agglomeration under both synthesis

and catalysis conditions remains a great challenge. The in-depth insight into the formation mechanism of single-atom catalysts is rarely reported [23–26].

Fe single-atom catalysts with four-coordinated FeN₄ structure embedded in carbon support represent the highest intrinsic ORR activity among various non-precious metal candidates because of the suitable binding strength with oxygen-containing intermediates [27–32]. However, the Fenton reaction has generally puzzled Fe-based catalysts causing severe activity degradation and thus insufficient stability [33–35]. Nevertheless, the overall ORR performances of Fe single-atom catalyst can be further promoted by adjusting the unsaturated coordination environment of isolated Fe active sites [36–40]. Meanwhile, the atomic-level dispersity of Fe single-atom catalysts is highly desirable in absence of any other forms of Fe species, such as Fe nanoparticles, to ensure efficient four-electron reaction efficiency in ORR catalysis. Therefore, enormous research has been dedicated to preparing high-performance Fe single-atom catalysts. The high-temperature pyrolysis of iron-containing polymer precursors has been predominantly developed [30, 41–43]. However, the chemical state evolution of Fe

* Corresponding authors.

E-mail addresses: yqzhu@bit.edu.cn (Y. Zhu), cbcao@bit.edu.cn (C. Cao).

<https://doi.org/10.1016/j.apcatb.2023.122675>

Received 25 October 2022; Received in revised form 3 January 2023; Accepted 21 March 2023

Available online 23 March 2023

0926-3373/© 2023 Elsevier B.V. All rights reserved.

species before converting into atomically dispersed Fe sites is rarely understood in depth. Therefore, it is urgently required to scientifically understand the effect of Fe species including Fe ions, oxides, and hydroxides in precursors on the formation of isolated Fe sites to provide reasonable guidance for controllably fabricating Fe single-atom catalysts.

Here, we report a solvent-mediated oxidative polymerization strategy to synthesize Fe single-atom catalysts embedded in porous nitrogen-doped carbon matrix (Fe-SA/PNC). In this strategy, the oxidative Fe^{3+} ions are purposefully applied as polymerization initiators and dopants in converting pyrrole monomer into polypyrrole, avoiding the potential dangers related to the removal of the hard template using HF or a hot alkaline solution treatment. Microscopic and spectroscopic characterizations demonstrate single isolated Fe atoms coordinated with nitrogen in FeN_4 moiety. Impressively, the as-prepared Fe-SA/PNC performs superior alkaline ORR activity with 0.90 V_{RHE} half-wave potential ($E_{1/2}$), more positive than that of Pt/C and previously reported non-precious metal counterparts. When assembled into Zn-air batteries as the air

electrode, Fe-SA/PNC exhibits high open circuit potential (1.68 V) and excellent operating durability with extraordinary ultra-long cycling stability over repeated 9000 cycles (over 1500 h). Our mechanistic investigation reveals that the reaction kinetics of oxidative Fe^{3+} ions with the predesigned solvent molecules in pyrrole polymerization determines the Fe transition state in polypyrrole and thus the final Fe products in pyrolytic catalysts. DFT calculations suggest that the abundant graphitic nitrogen surrounding FeN_4 active sites can change the charge distribution of Fe atoms towards higher ORR activity. The present findings enlighten fundamental understanding of the formation mechanism of Fe single-atom catalysts.

2. Experimental section

2.1. Preparation of Fe-SA/PNC

The Fe-SA/PNC was synthesized through a solvent-mediated chemical oxidative polymerization process. Firstly, 0.404 g $\text{Fe}(\text{NO}_3)_3 \cdot 9\text{H}_2\text{O}$

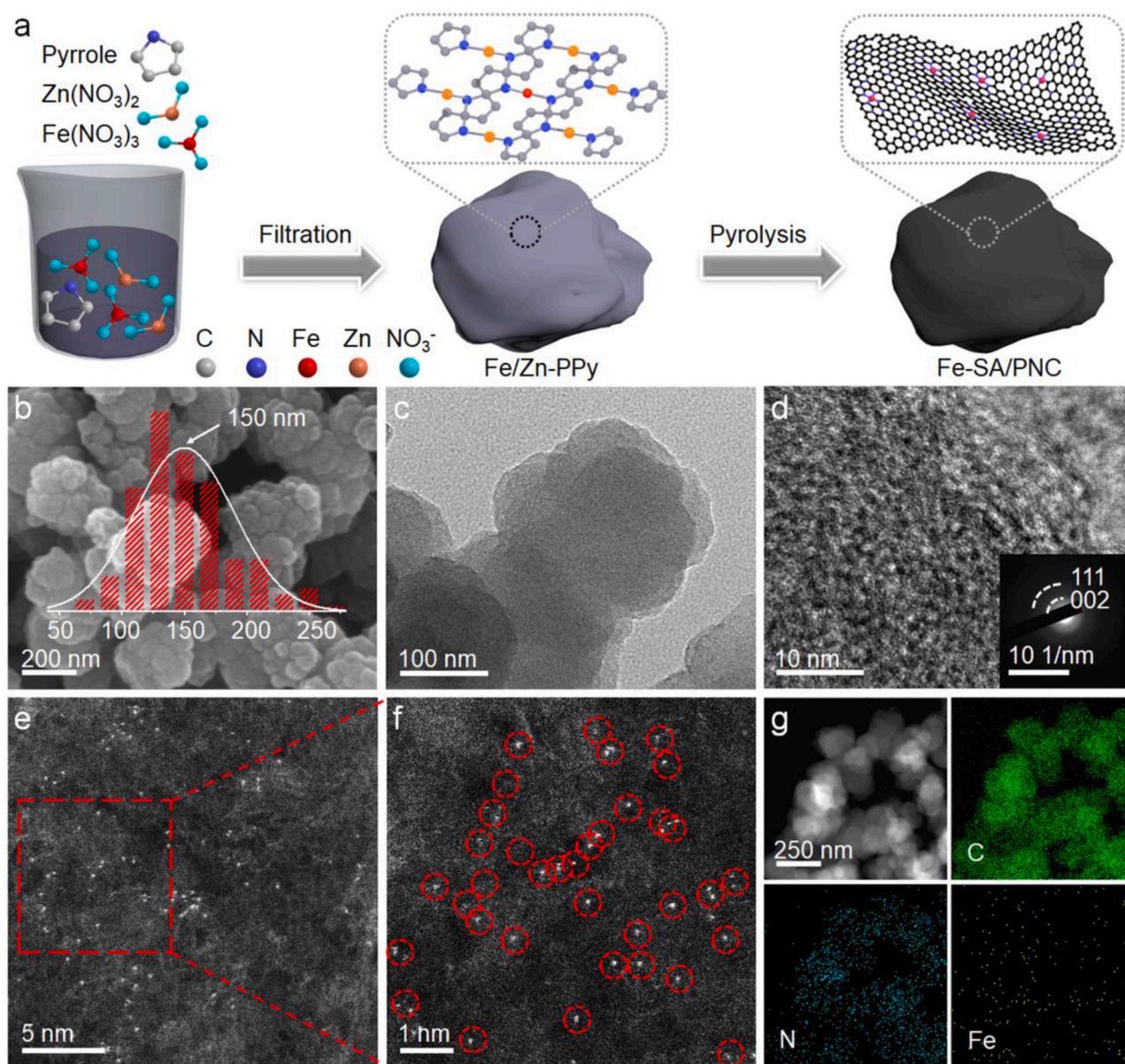


Fig. 1. Mechanistic diagram and characterizations of Fe-SA/PNC. (a) Schematic illustration of preparation process. (b) Typical FE-SEM image and inset showing the statistical particle size distribution. (c) TEM image. (d) HR-TEM image and SAED pattern. (e) and (f) AC-STEM image and enlarged view with Fe single atoms circled in red. (g) STEM image and corresponding EDX elemental mapping.

and 5.948 g $\text{Zn}(\text{NO}_3)_2 \cdot 6 \text{H}_2\text{O}$ (molar ratio of $\text{Fe}:\text{Zn} = 1:20$) were dissolved into 60 mL methanol solution and then stirred evenly (400 rpm). Secondly, 560 μL pyrrole monomer was added dropwise into the aforementioned methanol solution and intensely stirred for 2 h. Subsequently, the Fe-Zn/PPy composite precursors were collected by filtration and successively washed with deionized water and ethanol, and dried overnight. The final Fe-SA/PNC was obtained by high-temperature pyrolysis of Fe-Zn/PPy precursors at 900 °C under Ar flow for 3 h in a tube furnace with the heating rate of 5 °C min^{-1} .

3. Results and discussion

3.1. Synthesis and identification of Fe-SA/PNC

Fe-SA/PNC was synthesized by a solvent-mediated chemical oxidative polymerization method as illustrated in Fig. 1a. The oxidative Fe^{3+} ions are purposefully applied as polymerization initiators and dopants in converting pyrrole monomer into polypyrrole in methanol solution to form a polymer precursor (Fe/Zn-PPy). Subsequently, Fe/Zn-PPy precursor are pyrolyzed into Fe-SA/PNC. The presence of ZnCl_2 in precursor solution could separate the Fe ions to form cluster. In addition, Zn species is used as porogenic agent in polymerization and carbonization [44–46]. The Fe-SA/PNC displays a monodispersed sphere-like

configuration with an average diameter of 150 nm (Fig. 1b and Fig. S1a, b). Similarly, Fe/N-doped carbon (Fe/NC), porous N-doped carbon (PNC) and N-doped carbon (NC) also show a similar morphology (Fig. S2). Transmission electron microscopy (TEM) image (Fig. 1c and Fig. S1c,d) clearly reveals nanosphere structure of Fe-SA/PNC without iron nanoparticles. High-resolution TEM (HR-TEM) image presents irregular fringes, indicative of a disordered carbon structure, and no any fringes of iron nanocrystals are observed (Fig. 1d). The inset selected area electron diffraction pattern (SAED) exhibits typical graphitic carbon planes. Aberration-corrected scanning transmission electron microscopy (AC-STEM) image (Fig. 1e) demonstrates that the atomically dispersed Fe sites are well distinguished as the bright spots embedded in carbon matrix. Some isolated Fe single atoms are remarked by red circles in an enlarged AC-STEM image for close observation (Fig. 1f). The energy-dispersive X-ray (EDX) elemental mapping (Fig. 1g) reveals uniform distribution of Fe, N and C elements over Fe-SA/PNC and no cluster district of iron nanoparticles is discovered.

Fe-SA/PNC presents the similar X-ray diffraction (XRD) pattern to that of carbon-based counterparts (Fig. 2a) [47,48]. No any diffraction peaks are identified to metal Fe crystal. The Fe content is 0.4 wt% (Table S1). X-ray photoelectron spectroscopy (XPS, Fig. 2b and Fig. S3–7) suggests that nitrogen species in these samples are present in form of pyridinic N, pyrrolic N or Fe-N, graphitic N, and oxidized N,

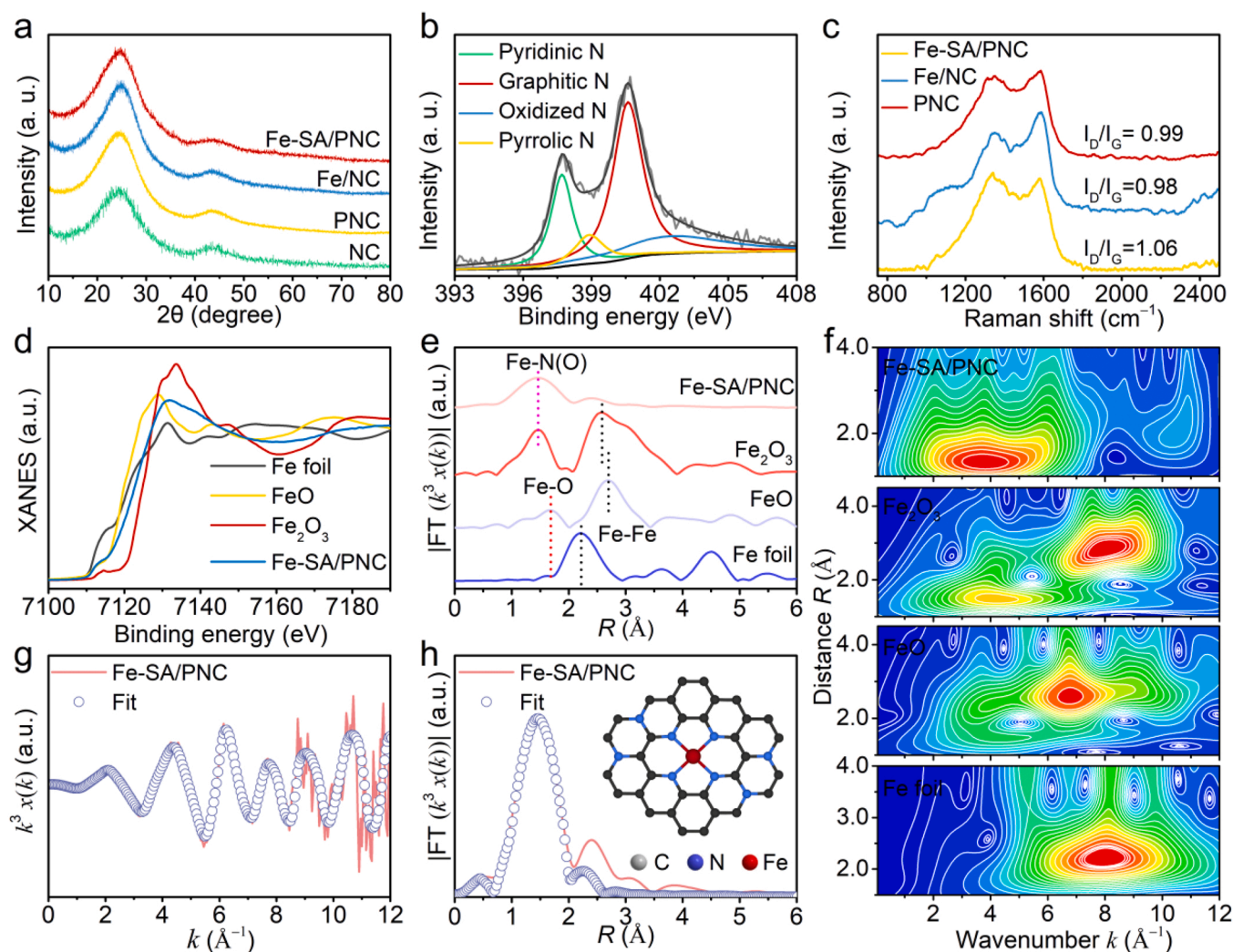


Fig. 2. Chemical composition and local atomic structure of Fe-SA/PNC. (a) XRD patterns. (b) High-resolution N 1s XPS spectrum. (c) Raman spectra. (d) Fe K-edge XANES spectra. (e) Fourier-transform (FT) of k^3 -weighted $\chi(k)$ -function of Fe K-edge EXAFS spectra. (f) Morlet wavelet images of Fe K-edge EXAFS signals. (g) k -space EXAFS fitting curve. (h) FT-EXAFS fitting curve in R space and inset showing schematic isolated Fe moiety.

respectively [49,50]. The N content of Fe-SA/PNC, Fe/NC, PNC, and NC are measured to be 8.27, 8.64, 7.63, and 7.53 at%, respectively, revealing that polypyrrole pyrolysis could generate rich nitrogen content, especially graphitic nitrogen (Table S1,S2). The pyridinic N can coordinate iron atoms to construct Fe-N_x configuration and the graphitic N is favorable for electron transfer in carbon skeleton [51,52]. Raman spectra (Fig. 2c) reveal a *sp*²-hybridized graphitization structure with rich defect of the three samples. Fe-SA/PNC exhibits obvious porous feature and much higher Brunauer–Emmett–Teller (BET) specific surface area of 205.00 m² g^{−1} compared with Fe/N-doped carbon (Fe/NC, 85.91 m² g^{−1}) and porous N-doped carbon (PNC, 106.08 m² g^{−1}) (Fig. S8 and Table S3). The porous structure is mainly attributed to the zinc evaporation during pyrolysis process [44,45].

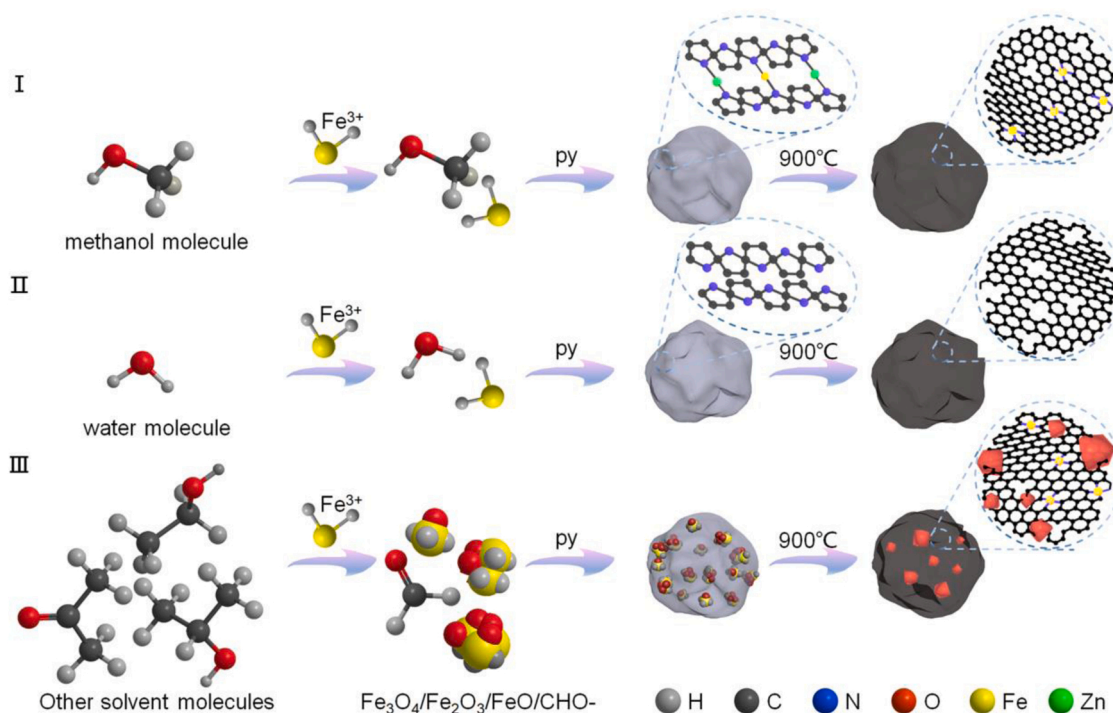
The normalized Fe K-edge X-ray absorption near edge structure spectroscopy (XANES) curves show that Fe-SA/PNC delivers relatively smooth XANES outline, obviously different from those of the references (Fig. 2d). The absorption edge position of Fe-SA/PNC is located between those of FeO and Fe₂O₃ counterparts, indicative of a charged positive state of Fe species in Fe-SA/PNC with unique electronic structure. The pre-edge peak of Fe-SA/PNC is attributable to 1s-4p_z transition as a fingerprint of four-coordinated FeN₄ structure. Fourier transformed extended X-ray absorption fine structure spectroscopy (FT-EXAFS) at Fe K-edge (Fig. 2e) reveal a predominant peak at 1.47 Å, which should be attributed to the scattering pair between central Fe species and nearby coordinated light atoms. By contrast, the FeO and Fe₂O₃ counterparts show multiple peaks, indicating Fe-O and Fe-Fe coordination shells. The first main peak of Fe₂O₃ reference related to the Fe-O coordination shell is also present at 1.47 Å. Accordingly, the predominant peak of Fe-SA/PNC should be ascribed to the Fe-N/C coordination shell. The standard Fe foil shows a sharp main peak located at 2.2 Å, being ascribed to the metallic Fe-Fe coordination. For Fe-SA/PNC, the peak at 2.2 Å is nearly negligible and without other high coordination shell peaks present, which suggests that Fe species is atomically dispersed.

Additionally, the wavelet transforms (WT) of Fe K-edge EXAFS oscillations were performed to provide much more powerful resolution in both *k* and *R* spaces for distinguishing the detailed atomic configuration of Fe-SA/PNC as shown in Fig. 2f. Based on the Fe-N/C coordination

contributions, the WT contour plots of Fe-SA/PNC only generate one maximum intensity point at 3.82 Å^{−1}, no maximum intensity point corresponding to Fe-Fe coordination can be discovered in comparison with that of Fe foil, FeO and Fe₂O₃ references. The WT contour plots evidently demonstrate the atomically dispersed feature of Fe species in Fe-SA/PNC. The least-square EXAFS fitting was quantitatively performed to extract the structural parameters of central Fe atom in Fe-SA/PNC. Fig. 2g,h demonstrate the well-matched fitting curves with experiment spectra. The present oscillations in *k* spaces are ascribed to scattering effect from nearby coordinated atoms to absorbing Fe atoms. The predominant peak should be attributed to Fe-N coordination shell, different from that of Fe foil (Fig. S9). The local atom structure of central Fe species in Fe-SA/PNC can be accordingly constructed as shown in the inset with coordination number of four and mean bond length of 1.98 Å (Table S4).

3.2. Mechanistic investigation of solvent-mediated oxidative polymerization

The formation of atomically dispersed Fe sites is dependent on the predesigned solvent molecules in the chemical oxidative polymerization strategy. Five solvents including methanol, ethanol, isopropanol, acetone, and water were adopted to investigate the solvent effect. As shown in Scheme 1, the oxidative Fe³⁺ ions can initiate and promote the polymerization of pyrrole and are spatially confined in the polypyrrole network in atomically isolated Fe state in methanol solvent. Finally, the confined Fe species are converted into Fe single-atom catalysts after pyrolysis. However, in ethanol, isopropanol, and acetone solvents, Fe³⁺ ions are translated into iron oxide and hydroxide nanoparticles by the redox reaction with solvent molecules and embedded in polypyrrole and finally converted into Fe nanoparticles. The water system just proceeds to porous N-doped carbon without Fe species. Field emission scanning electron microscope (FE-SEM) images (Fig. S10-11) reveal varying morphologies of the polypyrrole precursors and their relevant carbon products. Especially, the isopropanol solvent generates disordered carbon materials with notable Fe particles (Fig. S12). TEM images (Fig. S13-14) suggest that amount of small iron oxide nanoparticles can be clearly



Scheme 1. Schematic illustration of the solvent-mediated chemical oxidative polymerization process to construct Fe-SA/PNC.

distinguished in the polypyrrole precursors in ethanol, isopropanol, and acetone systems. However, no iron nanoparticles can be observed in the polypyrrole precursors in methanol and water systems. XRD patterns (Fig. S15) evidently suggest that iron oxide and hydroxide phases have been generated in pyrrole polymerization and are embedded in polypyrrole network before pyrolysis in isopropanol and acetone routes. Similarly, there are no Fe signal peak intensity in methanol, and water system due to low metal content before pyrolysis, whereas the content of Fe^{3+} in ethanol, isopropanol, and acetone can be reduced step by step, meanwhile the content of Fe^{2+} increases gradually (Fig. S16–17). After pyrolysis, the crystalline metal Fe phases can be clearly observed in ethanol, isopropanol, and acetone routes (Fig. S18–19).

The kinetics investigations (Fig. S20–23) of the redox reaction between trivalent Fe^{3+} ions and these five solvents suggest that their reaction rates follow the order acetone > isopropanol > ethanol > methanol > water. Therefore, the oxidative Fe^{3+} ions are partially reduced into Fe^{2+} ions by solvent molecules with different reaction kinetics. In particular, the redox reaction can convert alcoholic hydroxyl groups in methanol, ethanol, and isopropanol molecules into aldehyde groups (Fig. S21). The generated Fe^{2+} ions are more likely to produce iron oxide and hydroxide nanoparticles and embedded in polypyrrole network along with the oxidative polymerization of pyrrole. Therefore, the final dispersion state of Fe species in the pyrolytic carbon materials is significantly decided by the solvent effect in pyrrole polymerization. Furthermore, the atomically dispersed Fe sites naturally exhibit their superiority in ORR performances as shown in Fig. S24.

3.3. Oxygen reduction reaction over Fe-SA/PNC

The superior ORR activity of Fe-SA/PNC catalyst was further investigated by electrochemical measurements. Cyclic voltammograms (CV) curves of Fe-SA/PNC (Fig. 3a) reveal a strong oxygen reduction peak at $0.90 \text{ V}_{\text{RHE}}$ with intense cathodic current of 3.15 mA cm^{-2} , which are superior to that of Pt/C catalyst ($0.84 \text{ V}_{\text{RHE}}$ and 0.56 mA cm^{-2} , Fig. S25). Linear sweep voltammetry (LSV, Fig. 3b) confirms that Fe-SA/PNC presents the most positive onset potential of $0.94 \text{ V}_{\text{RHE}}$ at -1.00 mA cm^{-2} among the synthesized catalysts and Pt/C ($0.90 \text{ V}_{\text{RHE}}$). Fe-SA/PNC displays an outstanding $E_{1/2}$ of $0.90 \text{ V}_{\text{RHE}}$, which significantly surpasses that of Fe/N-doped carbon (Fe/NC), porous N-doped carbon (PNC), N-doped carbon (NC), Pt/C ($0.84 \text{ V}_{\text{RHE}}$) and many recently reported ORR catalysts (Fig. 3c, and Table S5). Moreover, Fe-SA/PNC exhibits 3.52-fold enhancement of J_k value at $0.90 \text{ V}_{\text{RHE}}$ compared to Pt/C. However, Fe-SA/PNC displays relatively lower ORR property in acidic media (Fig. S26) compared to the Pt/C. The superior alkaline ORR activity of Fe-SA/PNC catalyst should be ascribed to the unique atomically dispersed Fe sites. In addition, according to the ORR performance and Zn content at different calcination temperature, the major active sites in Fe-SA/PNC are FeN_4 centers instead of Zn species (Fig. S27 and Table S6).

Tafel plots were extracted to evaluate the kinetic behaviours of the above-mentioned catalysts. As summarized in Fig. 3d, the Tafel slope of Fe-SA/PNC is only 74 mV dec^{-1} , lower than that of Pt/C (75 mV dec^{-1}), Fe/NC (153 mV dec^{-1}), PNC (203 mV dec^{-1}), and NC (225 mV dec^{-1}).

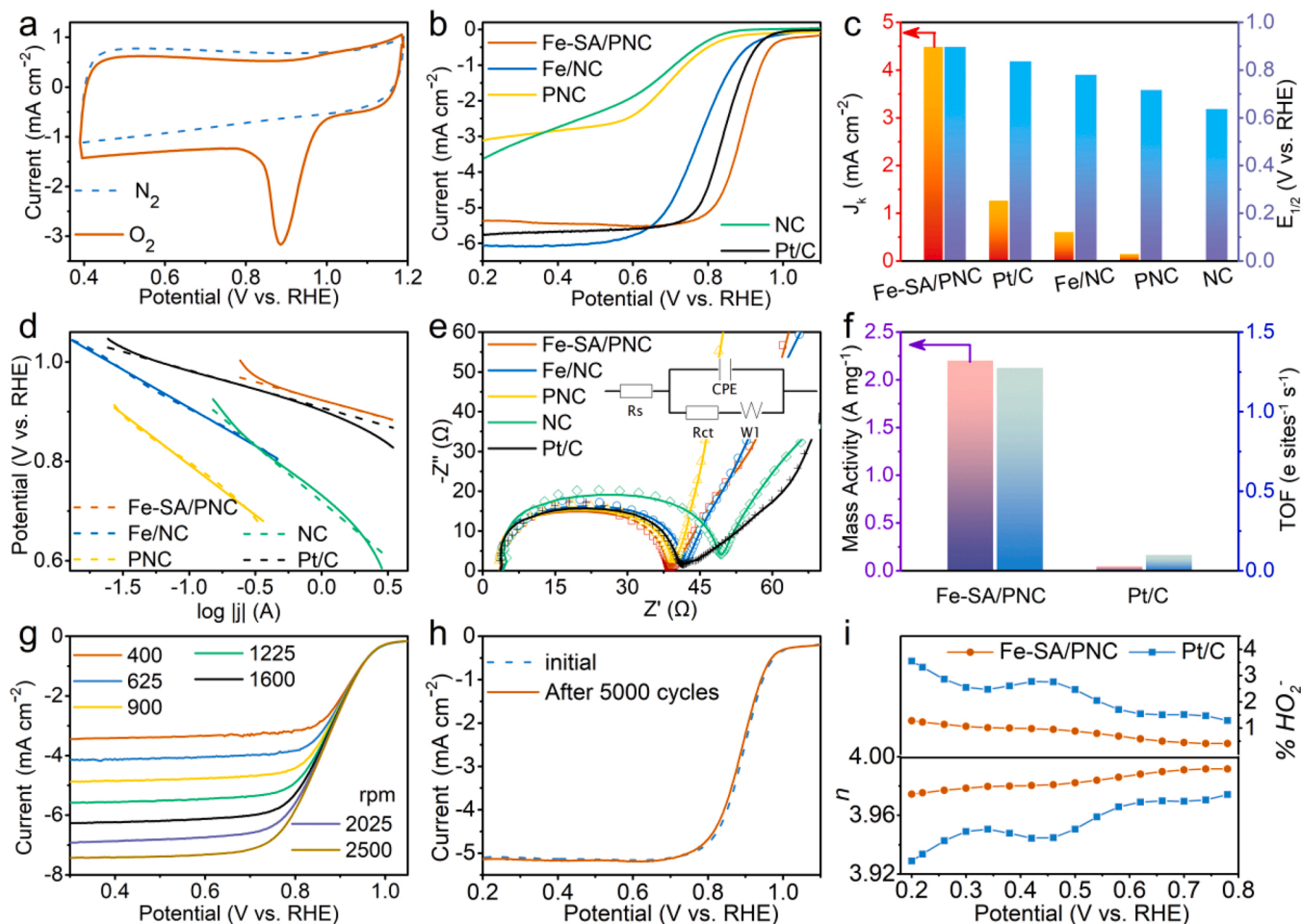


Fig. 3. ORR performances of Fe-SA/PNC. (a) CV curves in O_2 - and N_2 -saturated 0.1 M KOH electrolyte. (b) LSV curves under 10 mV s^{-1} scan rate at 1600 rpm. (c) J_k at $0.90 \text{ V}_{\text{RHE}}$ and $E_{1/2}$. (d) Tafel slopes at 1600 rpm. (e) EIS curves. (f) Mass activities and turnover frequency at $0.90 \text{ V}_{\text{RHE}}$. (g) LSV curves at various rotating rates. (h) LSV curves before and after repeated 5000 CV cycles. (i) H_2O_2 yield and electron-transfer number plots.

The larger J_k value and the lower Tafel slope of Fe-SA/PNC demonstrate an excellent ORR kinetics. The electrochemical impedance spectroscopy (EIS, Fig. 3e) suggests that Fe-SA/PNC displays a smaller x-intercept, indicating lower internal and electrode/electrolyte surface resistance [53]. Besides, the steeper slope at low-frequency range reveals a faster mass diffusion due to the porous structures [54,55]. As shown in Fig. 3f, Fe-SA/PNC can deliver a large mass activity (MA) of 2.21 A mg^{-1} at $0.90 \text{ V}_{\text{RHE}}$, which is 44.2 times higher than that of Pt/C, implying high specific activity over Fe-SA/PNC. In order to test the activity of FeN_4 active sites, the corresponding TOF was calculated. The turnover frequency (TOF) of Fe-SA/PNC ($1.28 \text{ e site}^{-1} \text{ s}^{-1}$) is 12.8 times larger than that of Pt/C and even surpasses other reported catalysts so far (Table S7). The remarkable MA and TOF values of Fe-SA/PNC demonstrate an unexpectedly excellent FeN_4 catalytic performances. The LSV plots at different rotating rates were collected to confirm the ORR pathway over Fe-SA/PNC catalyst. As shown in Fig. 3g, Fe-SA/PNC exhibits steady onset potentials and stair-stepping limited current density at various rotating rates. The average electron-transfer number (n) of Fe-SA/PNC is evaluated to be 4.09, which is approaching to the theoretical value of 4 and indicative of a four-electron oxygen reduction pathway (Fig. S28). The accelerated durability test (ADT) was conducted to examine the long-term cycling stability of Fe-SA/PNC. As shown in Fig. 3h, Fe-SA/PNC can maintain nearly the same half-wave potential value after repeated 5000 cycles, whereas 64 mV decay in half-wave potential is observed in Pt/C catalyst under the identical

testing condition (Fig. S29). Therefore, Fe-SA/PNC possesses excellent durability in the alkaline electrolyte. The rotating ring disk electrode (RRDE) measurements (Fig. 3i and Fig. S30) demonstrate extremely low H_2O_2 yield below 1.3% $\text{HO}_2\%$ of Fe-SA/PNC, corresponding with a four-electron ORR passageway ($n = 3.98$). The tolerance toward methanol corrosion of electrocatalyst in ORR process is of significant importance for practical applications. Hence, the methanol tolerance of Fe-SA/PNC was evaluated by i-t measurement in an O_2 -saturated 0.1 M KOH electrolyte with 1.0 M methanol. Fe-SA/PNC can maintain catalytic stability of 92.8% current retention after methanol injection as that before (Fig. S31). The result demonstrates excellent methanol tolerance of Fe-SA/PNC. Surprisingly, Fe-SA/PNC performs a modest overpotential above 635 mV at 10 mA cm^{-2} toward oxygen evolution reaction (Fig. S32).

3.4. Electrochemical Performances of Fe-SA/PNC in Zn-air Batteries

Fe-SA/PNC was further evaluated as the cathode materials for Zn-air batteries. The structural model of the home-made Zn-air battery (ZAB) is shown in Fig. 4a. One single Fe-SA/PNC-assembled Zn-air battery can successfully power a light bulb with remarkable operation stability over 4 h (Fig. 4b). The higher open circuit voltage (OCV) of Fe-SA/PNC-assembled Zn-air battery is achieved at 1.68 V and maintained above 1.55 V after 8 h compared with Pt/C (Fig. 4c). The inset shows the corresponding photography of the Fe-SA/PNC-assembled Zn-air battery

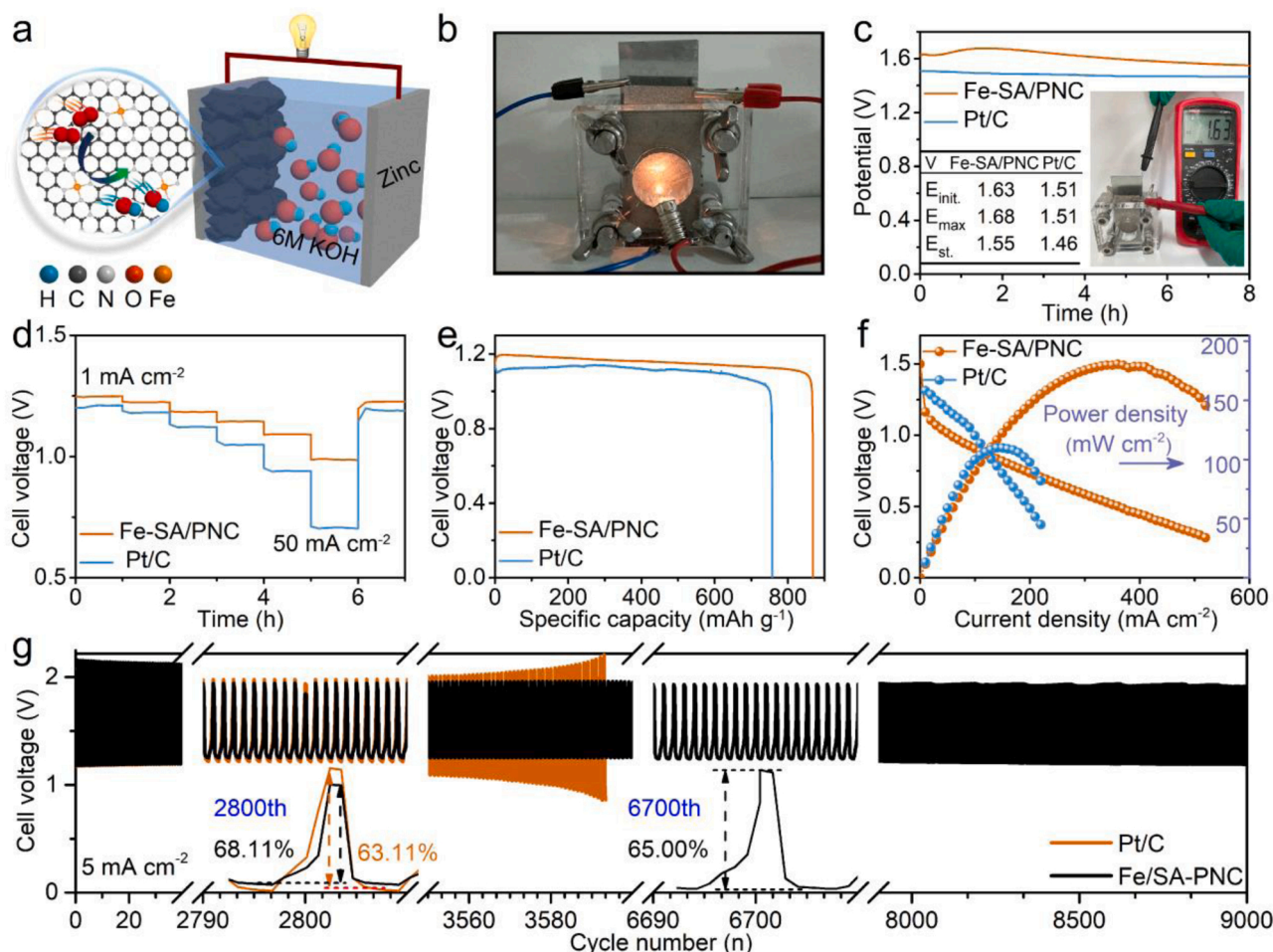


Fig. 4. Zn-air battery performances of Fe-SA/PNC. (a) Schematic diagram of Zn-air battery. (b) Photograph of a lighted light bulb (1.5 V, 0.2 A) powered by one liquid Fe-SA/PNC-assembled battery. (c) Open circuit curves and inset showing photograph of Fe-SA/PNC-based ZAB with measured open-circuit voltage and table of initial, maximum, and stable open circuit voltage. (d) Discharge profiles at various current densities. (e) Specific capacities curves at 5 mA cm^{-2} . (f) Discharge polarization profiles and the corresponding power density plots. (g) Cycling stability.

and the measured OCV value. Electrochemical impedance spectroscopy (EIS) reveals that the high open circuit voltage is related to the internal battery resistance: the low faradaic charge-transfer resistance and high gas diffusion resistance (Fig. S33, 34 and Table S8). At 1, 2, 5, 10, 20, 50 mA cm⁻² current densities, Fe-SA/PNC-based air cathode can deliver stable voltage plateaus at 1.25, 1.23, 1.18, 1.15, 1.09 and 0.99 V, respectively, which are superior to that of Pt/C (Fig. 4d). After current density restoring to 1 mA cm⁻², Fe-SA/PNC-based air cathode shows the similar voltage plateau at 1.23 V as initial state, indicative of a potential discharge stability. Fe-SA/PNC can achieve a high specific capacity of 868 mAh g⁻¹ (928 Wh kg⁻¹ energy density, Fig. 4e). Fig. 4f shows a comparison of discharge polarization curves and the corresponding power density plots of Fe-SA/PNC and Pt/C electrodes. The Pt/C electrode achieves 110 mW cm⁻² peak power density at 150 mA cm⁻², slightly lower than that of the Fe-SA/PNC (180.5 mW cm⁻² at 360 mA cm⁻²).

Fe-SA/PNC cathode also shows a narrow charge/discharge overpotential gap of 0.58 V, which might be influenced by the high open circuit potential, surpassing that of Pt/C (0.79 V) and recently reported ZABs (Fig. 4g and Table S5). Furthermore, Fe-SA/PNC-based air cathode can maintain nearly unchanged voltage gap over 9000 cycles (1500 h, i. e., >62.5 days,) with a high energy efficiency of 68.11% at the 2800th cycle and 65% at the 6700th cycle, which are highly competitive to Pt/C (63.11% at the 2800th cycles). The fitting EIS plots elucidate that the electrolyte resistance (R_e) and faradaic charge-transfer resistance (R_{ct}) increase with the cycling test (Fig. S35, and Table S9). To further investigate the structural evolution upon cycling, XRD, SEM and TEM analysis were operated on the Fe-SA/PNC-based air cathode cycled over 9000 cycles (Fig. S36-40). The surface of the sphere-like nanoparticles becomes rougher with a lot of wrinkles, but there is no obvious

aggregation of Fe nanoparticles, which confirms the structural robustness of Fe-SA/PNC. Moreover, abundant inactive potassium carbonate is generated after long periods of alternating redox reactions, that could deteriorate the cycling stability. In addition, SCN⁻, with strong affinity to Fe, proved that the real active sites in Zn-air battery are Fe single atoms (Fig. S41, and Table S10). These results demonstrate an excellent cycling stability of Fe-SA/PNC-based air cathode, which is mainly related to the robust sphere-like morphology and the FeN₄ structure [8]. Therefore, Fe-SA/PNC can be exploited as a robust electrocatalyst alternative for long-life rechargeable zinc-air batteries.

3.5. Theoretical ORR investigation over Fe-SA/PNC

Density functional theory (DFT) calculations were performed to investigate the effect of adjacent non-coordinated graphitic nitrogen on the electronic conductivity and ORR activity of Fe-SA/PNC catalyst. The optimized atomic structural model for Fe-SA/PNC was constructed as shown in Fig. 5a (denoted as FeN₄-4 N), in which four non-coordinated graphitic nitrogen atoms were introduced into the regular four-coordinated FeN₄ structure and symmetrically located around FeN₄ sites. The regular FeN₄ model was used as the control structure (Fig. S42). Charge density analysis (Fig. 5b and Fig. S43) reveals apparent charge transfer from Fe to N atoms, leading to positively charged state of Fe species, which is favorable for O₂ adsorption [56]. Similarly, the projected density of states (PDOS) of Fe 3d orbitals results also suggest that the *d*-band center of FeN₄-4 N is increased to -1.49 eV in comparison with that -1.56 eV of FeN₄ (Fig. 5c), indicative of the coordination contribution from adjacent non-coordinated graphitic nitrogen atoms. The state density of active Fe center can be regulated by adjacent non-coordinated graphitic nitrogen. The sharp PDOS peaks

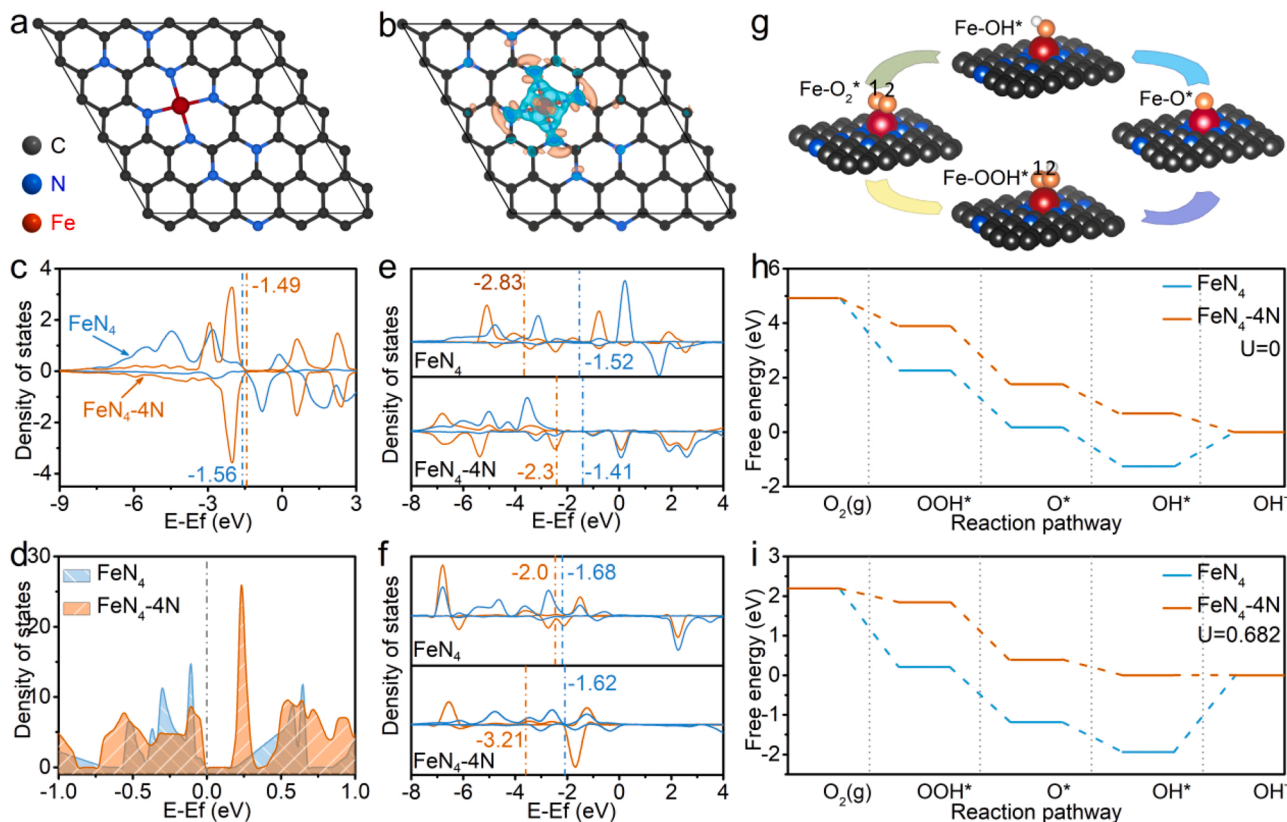


Fig. 5. Theoretical ORR activity of Fe-SA/PNC. (a) and (b) Optimized structural model and charge density of FeN₄-4 N sites in Fe-SA/PNC. (c) The projected density of states (PDOS) for Fe 3d orbitals of FeN₄ and FeN₄-4 N, dotted line showing the relevant Fe 3d band center. (d) The PDOS of 3d orbitals of Fe atoms, black line indicating the Fermi level. (e) and (f) The calculated density of states of O₂* adsorption and OH* desorption state. The Fe 3d and O 2p band centers are marked as blue and orange dotted lines for each sample. (g) Four-electron ORR process over FeN₄-4 N. (h) and (i) Free-energy diagram of ORR reaction pathways with different equilibrium potential (U).

suggest a vacant orbital near the Fermi level, which is conducive to adsorbing O₂ (Fig. S44b). Therefore, the introducing of four graphitic nitrogen could modulate the electronic structure and charge density of active Fe centers. The PDOS of Fe 3d orbitals (Fig. 5d and Fig. S45) display the significantly decreased gap between valence and conduction band. The obvious increased charge density can result the enhanced electronic conductivity of FeN₄-4 N [57,58].

The bond strength toward adsorbed intermediates over active Fe centers can also be determined by the filling of anti-bonding state near Fermi level [59]. For O₂ adsorption state, the Fe 3d band matches well with the O 2p band (Fig. S46-49), indicating a strong electronic coupling in FeN₄-4 N-O₂ * pair. By contrast, FeN₄ is unlikely to interact with O₂ because the d_{x²-y²} orbital remains unoccupied at high energy state (Fig. S50-52). As for OH⁻ dissociation state, the O 2p_x-band is sharp and narrow, and remains unoccupied with the Fe 3d-band, inducing a weak electronic coupling between FeN₄-4 N and OH⁻ (Fig. S53-59). The distance between Fe 3d and O 2p band center was further calculated to investigate the influence of four graphitic nitrogen on these two processes. For the first step to absorb O₂ (Fig. 5e), the distance in FeN₄-4 N is smaller than that in FeN₄, showing full overlap between Fe 3d and O 2p orbitals, which deems to bond O₂ strongly [60]. As for OH⁻ dissociation state (Fig. 5f), FeN₄-4 N structure presents much more slightly overlapped Fe 3d and O 2p orbitals, resulting in a lower energy barrier for desorbing OH⁻.

The four-electron ORR process over single Fe atom in FeN₄-4 N is proposed as shown in Fig. 5g including adsorption and dissociation of reaction intermediates. In the first step, Fe atom adsorbs oxygen molecule to form Fe-O₂ * bond with bond length of 1.93 Å in FeN₄-4 N, which is shorter than that of Fe-O₂ * bond (2.03 Å) in FeN₄, suggesting stronger bonding interaction with oxygen and thus better ORR activity and stability of FeN₄-4 N (Fig. S60-62, and Table S11). The free-energy profiles over FeN₄ and FeN₄-4 N in an alkaline solution (pH=13) are displayed in Fig. 5h,i and Fig. S63 (ESI[†]). The detailed reaction energetics are calculated in Supplementary Table S12-13. At U = 0 V, the four-electron ORR processes are exothermic reactions over FeN₄-4 N in view of the fact that the free-energy profile is downhill. The rate determining step (RDS) on FeN₄ and FeN₄-4 N are the last OH⁻ desorption step, which exhibit the absolute value of free energy variations (|ΔG|) of 0.682 and 1.258 eV, respectively. The much smaller |ΔG| (0.682 eV) value for FeN₄-4 N demonstrates that the introduction of graphitic nitrogen can boost the ORR performance. Therefore, the introducing of four graphitic nitrogen atoms can promote the O₂ adsorption and OH⁻ desorption processes in Fe-SA/PNC and essentially enhance electronic conductivity, which demonstrates a favorable role in catalyzing the ORR.

4. Conclusions

In summary, a solvent-mediated oxidative pyrrole polymerization strategy is developed to reveal the mechanistic formation of isolated Fe sites in Fe-SA/PNC catalyst. The final chemical state of Fe species is highly dependent on the reaction kinetics of oxidative Fe³⁺ ions with solvent molecules in pyrrole polymerization process. The as-synthesized Fe-SA/PNC can show superior ORR activity in alkaline media. When assembled in Zn-air batteries as the air electrode, Fe-SA/PNC exhibits high open circuit potential (1.68 V) and superior cycling stability (over 9000 cycles, above 1500 h, i.e., >62.5 days). DFT calculations suggest that the introduction of four graphitic nitrogen around active Fe center can inherently improve electronic conductivity and accelerate O₂ adsorption and OH⁻ desorption in Fe-SA/PNC. This work highlights a theoretical guideline for synthesizing atomically dispersed Fe catalysts towards the sustainable application of energy storage and conversion devices.

CRediT authorship contribution statement

Xiuyun Yao: Conceptualization, Methodology, Investigation, Data curation, Validation, Writing – original draft, Writing – review & editing, Supervision. **Youqi Zhu:** Conceptualization, Supervision, Writing – review & editing. **Zhanli Han:** Data analysis. **Lifen Yang:** Data analysis. **Jiachen Tian:** Data analysis. **Tianyu Xia:** Data analysis. **Hui Peng:** Data analysis. **Chuanbao Cao:** Writing – review & editing, Supervision, Funding acquisition.

Declaration of Competing Interest

The authors declare that they have no known competing financial interests or personal relationships that could have appeared to influence the work reported in this paper.

Data Availability

Data are shared in supporting information.

Acknowledgements

This work was financed by the National Natural Science Foundation of China (21371023 and 52173273) and Fundamental Research Funds for the Central Universities (2022CX11013). We also thank the shiyanjia lab (www.shiyanjia.com) for the XPS test.

Appendix A. Supporting information

Supplementary data associated with this article can be found in the online version at doi:10.1016/j.apcatb.2023.122675.

References

- [1] Q. Wang, Q. Feng, Y. Lei, S. Tang, L. Xu, Y. Xiong, G. Fang, Y. Wang, P. Yang, J. Liu, W. Liu, X. Xiong, Quasi-solid-state Zn-air batteries with an atomically dispersed cobalt electrocatalyst and organohydrogel electrolyte, *Nat. Commun.* 13 (2022) 3689.
- [2] H. Lei, L. Ma, Q. Wan, Z. Huangfu, S. Tan, Z. Wang, W. Mai, Porous carbon nanofibers confined NiFe alloy nanoparticles as efficient bifunctional electrocatalysts for Zn-air batteries, *Nano Energy* 104 (2022), 107941.
- [3] J. Zhang, Z. Zhao, Z. Xia, L. Dai, A metal-free bifunctional electrocatalyst for oxygen reduction and oxygen evolution reactions, *Nat. Nanotechnol.* 10 (2015) 444–452.
- [4] A. Wang, X. Zhang, S. Gao, C. Zhao, S. Kuang, S. Lu, J. Niu, G. Wang, W. Li, D. Chen, H. Zhang, X. Zhou, S. Zhang, B. Zhang, W. Wang, Fast-charging Zn-air batteries with long lifetime enabled by reconstructed amorphous multi-metallic sulfide, *Adv. Mater.* 34 (2022) 2204247.
- [5] J. Guan, S. Yang, T. Liu, Y. Yu, J. Niu, Z. Zhang, F. Wang, Intermetallic FePt@PtBi core-shell nanoparticles for oxygen reduction electrocatalysis, *Angew. Chem. Int. Ed.* 133 (2021) 22070–22075.
- [6] N. Wang, J. Li, W. Sun, Y. Hou, L. Zhang, X. Hu, Y. Yang, X. Chen, C. Chen, B. Chen, W. Qian, Rational design of zinc/zeolite catalyst: selective formation of p-xylylene from methanol to aromatics reaction, *Angew. Chem. Int. Ed.* 134 (2022), e202114786.
- [7] Z. Lin, H. Huang, L. Cheng, W. Hu, P. Xu, Y. Yang, J. Li, F. Gao, K. Yang, S. Liu, P. Jiang, W. Yan, S. Chen, C. Wang, H. Tong, M. Huang, W. Zheng, H. Wang, Q. Chen, Tuning the p-orbital electron structure of s-block metal Ca enables a high-performance electrocatalyst for oxygen reduction, *Adv. Mater.* 33 (2021) 2107103.
- [8] D. Yuan, Y. Dou, Z. Wu, Y. Tian, K.-H. Ye, Z. Lin, S.-X. Dou, S. Zhang, Atomically thin materials for next-generation rechargeable batteries, *Chem. Rev.* 122 (2022) 957–999.
- [9] J. Li, Y.-f. Jiang, Q. Wang, C.-Q. Xu, D. Wu, M.N. Banis, K.R. Adair, K. Doyle-Davis, D.M. Meira, Y.Z. Finfrock, W. Li, L. Zhang, T.-K. Sham, R. Li, N. Chen, M. Gu, J. Li, X. Sun, A general strategy for preparing pyrrolic-N₄ type single-atom catalysts via pre-located isolated atoms, *Nat. Commun.* 12 (2021) 6806.
- [10] F. Wu, C. Pan, C.-T. He, Y. Han, W. Ma, H. Wei, W. Ji, W. Chen, J. Mao, P. Yu, D. Wang, L. Mao, Y. Li, Single-atom Co-N₄ electrocatalyst enabling four-electron oxygen reduction with enhanced hydrogen peroxide tolerance for selective sensing, *J. Am. Chem. Soc.* 142 (2020) 16861–16867.
- [11] Y. Chen, R. Gao, S. Ji, H. Li, K. Tang, P. Jiang, H. Hu, Z. Zhang, H. Hao, Q. Qu, X. Liang, W. Chen, J. Dong, D. Wang, Y. Li, Atomic-level modulation of electronic density at cobalt single-atom sites derived from metal-organic frameworks: enhanced oxygen reduction performance, *Angew. Chem. Int. Ed.* 60 (2021) 3212–3221.

- [12] Y. He, H. Guo, S. Hwang, X. Yang, Z. He, J. Braaten, S. Karakalos, W. Shan, M. Wang, H. Zhou, Z. Feng, K.L. More, G. Wang, D. Su, D.A. Cullen, L. Fei, S. Litster, G. Wu, Single cobalt sites dispersed in hierarchically porous nanofiber networks for durable and high-power PGM-free cathodes in fuel cells, *Adv. Mater.* 32 (2020) 2003577.
- [13] P. Wang, Y. Ren, R. Wang, P. Zhang, M. Ding, C. Li, D. Zhao, Z. Qian, Z. Zhang, L. Zhang, L. Yin, Atomically dispersed cobalt catalyst anchored on nitrogen-doped carbon nanosheets for lithium-oxygen batteries, *Nat. Commun.* 11 (2020) 1576.
- [14] J. Liu, J. Bak, J. Roh, K.-S. Lee, A. Cho, J.W. Han, E. Cho, Reconstructing the coordination environment of platinum single-atom active sites for boosting oxygen reduction reaction, *ACS Catal.* 11 (2020) 466–475.
- [15] W. Wu, Y. Liu, D. Liu, W. Chen, Z. Song, X. Wang, Y. Zheng, N. Lu, C. Wang, J. Mao, Y. Li, Single copper sites dispersed on hierarchically porous carbon for improving oxygen reduction reaction towards zinc-air battery, *Nano Res.* 14 (2021) 998–1003.
- [16] X. Li, H. Rong, J. Zhang, D. Wang, Y. Li, Modulating the local coordination environment of single-atom catalysts for enhanced catalytic performance, *Nano Res.* 13 (2020) 1842–1855.
- [17] C. Ma, Y. Zhang, Y. Feng, N. Wang, L. Zhou, C. Liang, L. Chen, Y. Lai, X. Ji, C. Yan, W. Wei, Engineering Fe–N coordination structures for fast redox conversion in lithium–sulfur batteries, *Adv. Mater.* 33 (2021) 2100171.
- [18] K. Yuan, D. Lützenkirchen-Hecht, L. Li, L. Shuai, Y. Li, R. Cao, M. Qiu, X. Zhuang, M.K.H. Leung, Y. Chen, U. Scherf, Boosting oxygen reduction of single iron active sites via geometric and electronic engineering: nitrogen and phosphorus dual coordination, *J. Am. Chem. Soc.* 142 (2020) 2404–2412.
- [19] Y. Wang, H. Su, Y. He, L. Li, S. Zhu, H. Shen, P. Xie, X. Fu, G. Zhou, C. Feng, D. Zhao, F. Xiao, X. Zhu, Y. Zeng, M. Shao, S. Chen, G. Wu, J. Zeng, C. Wang, Advanced electrocatalysts with single-metal-atom active sites, *Chem. Rev.* 120 (2020) 12217–12314.
- [20] Y. Chen, S. Ji, Y. Wang, J. Dong, W. Chen, Z. Li, R. Shen, L. Zheng, Z. Zhuang, D. Wang, Y. Li, Isolated single iron atoms anchored on N-doped porous carbon as an efficient electrocatalyst for the oxygen reduction reaction, *Angew. Chem. Int. Ed.* 56 (2017) 6937–6941.
- [21] A. Schoedel, M. Li, D. Li, M. O’Keeffe, O.M. Yaghi, Structures of metal-organic frameworks with rod secondary building units, *Chem. Rev.* 116 (2016) 12466–12535.
- [22] B. Hu, A. Huang, X. Zhang, Z. Chen, R. Tu, W. Zhu, Z. Zhuang, C. Chen, Q. Peng, Y. Li, Atomic Co/Ni dual sites with N/P-coordination as bifunctional oxygen electrocatalyst for rechargeable zinc-air batteries, *Nano Res.* 14 (2021) 3482–3488.
- [23] Y. Shao, X. Feng, L. Dai, J.-P. Dodelet, Advancing materials electrochemistry for chemical transformation, *Adv. Mater.* 31 (2019) 1903622.
- [24] G. Wu, P. Zelenay, Nanostructured nonprecious metal catalysts for oxygen reduction reaction, *Acc. Chem. Res.* 46 (2013) 1878–1889.
- [25] V. Nallathambi, J.-W. Lee, S.P. Kumaraguru, G. Wu, B.N. Popov, Development of high performance carbon composite catalyst for oxygen reduction reaction in PEM proton exchange membrane fuel cells, *J. Power Sources* 183 (2008) 34–42.
- [26] G. Wu, M. Nelson, S. Ma, H. Meng, G. Cui, P.K. Shen, Synthesis of nitrogen-doped onion-like carbon and its use in carbon-based CoFe binary non-precious-metal catalysts for oxygen-reduction, *Carbon* 49 (2011) 3972–3982.
- [27] L. Jiao, J. Li, L.L. Richard, Q. Sun, T. Stracensky, E. Liu, M.T. Sougrati, Z. Zhao, F. Yang, S. Zhong, H. Xu, S. Mukerjee, Y. Huang, D.A. Cullen, J.H. Park, M. Ferrandon, D.J. Myers, F. Jaouen, Q. Jia, Chemical vapour deposition of Fe–N–C oxygen reduction catalysts with full utilization of dense Fe–N₄ sites, *Nat. Mater.* 20 (2021) 1385–1391.
- [28] J. Li, S. Ghoshal, W. Liang, M.-T. Sougrati, F. Jaouen, B. Halevi, S. McKinney, G. McCool, C. Ma, X. Yuan, Z.-F. Ma, S. Mukerjee, Q. Jia, Structural and mechanistic basis for the high activity of Fe–N–C catalysts toward oxygen reduction, *Energ. Environ. Sci.* 9 (2016) 2418–2432.
- [29] H. Adabi, A. Shakouri, N. Ul Hassan, J.R. Varcoe, B. Zulevi, A. Serov, J. R. Regalbuto, W.E. Mustain, High-performing commercial Fe–N–C cathode electrocatalyst for anion-exchange membrane fuel cells, *Nat. Energy* 6 (2021) 834–843.
- [30] D.H. Kim, S. Ringe, H. Kim, S. Kim, B. Kim, G. Bae, H.-S. Oh, F. Jaouen, W. Kim, H. Kim, C.H. Choi, Selective electrochemical reduction of nitric oxide to hydroxylamine by atomically dispersed iron catalyst, *Nat. Commun.* 12 (2021) 1856.
- [31] J. Guo, B. Li, Q. Zhang, Q. Liu, Z. Wang, Y. Zhao, J. Shui, Z. Xiang, Highly accessible atomically dispersed Fe–N_x sites electrocatalyst for proton-exchange membrane fuel cell, *Adv. Sci.* 8 (2021) 2002249.
- [32] T. Marshall-Roth, N.J. Libretto, A.T. Wrobel, K.J. Anderton, M.L. Pegis, N.D. Ricke, T.V. Voorhis, J.T. Miller, Y. Surendranath, A pyridinic Fe–N₄ macrocycle models the active sites in Fe/N-doped carbon electrocatalysts, *Nat. Commun.* 11 (2020) 5283.
- [33] J. Hong, B. Wang, G. Xiao, N. Wang, Y. Zhang, A.Y. Khodakov, J. Li, Tuning the metal-support interaction and enhancing the stability of titania-supported cobalt fischer–tropsch catalysts via carbon nitride coating, *ACS Catal.* 10 (2020) 5554–5566.
- [34] G. Wu, K.L. More, C.M. Johnston, P. Zelenay, High-performance electrocatalysts for oxygen reduction derived from polyaniline, iron, and cobalt, *Science* 332 (2011) 443–447.
- [35] K. Strickland, E. Miner, Q. Jia, U. Tylus, N. Ramaswamy, W. Liang, M.-T. Sougrati, F. Jaouen, S. Mukerjee, Highly active oxygen reduction non-platinum group metal electrocatalyst without direct metal–nitrogen coordination, *Nat. Commun.* 6 (2015) 7343.
- [36] N. Ramaswamy, U. Tylus, Q. Jia, S. Mukerjee, Activity descriptor identification for oxygen reduction on nonprecious electrocatalysts: linking surface science to coordination chemistry, *J. Am. Chem. Soc.* 135 (2013) 15443–15449.
- [37] J. Li, F. Jaouen, Structure and activity of metal-centered coordination sites in pyrolyzed metal–nitrogen–carbon catalysts for the electrochemical reduction of O₂, *Curr. Opin. Electro* 9 (2018) 198–206.
- [38] M.J. Workman, A. Serov, L.-K. Tsui, P. Atanasov, K. Artyushkova, Fe–N–C catalyst graphitic layer structure and fuel cell performance, *ACS Energy Lett.* 2 (2017) 1489–1493.
- [39] J. Li, N. Wang, J. Tian, W. Qian, W. Chu, Cross-coupled macro-mesoporous carbon network toward record high energy-power density supercapacitor at 4 V, *Adv. Funct. Mater.* 28 (2018) 1806153.
- [40] Y. Ni, L. Lin, Y. Shang, L. Luo, L. Wang, Y. Lu, Y. Li, Z. Yan, K. Zhang, F. Cheng, J. Chen, Regulating electrocatalytic oxygen reduction activity of a metal coordination polymer via *d*– π conjugation, *Angew. Chem. Int. Ed.* 60 (2021) 16937–16941.
- [41] J. Li, M.T. Sougrati, A. Zitolo, J.M. Ablett, I.C. Oğuz, T. Mineva, I. Matanovic, P. Atanasov, Y. Huang, I. Zenyuk, A. Di Cicco, K. Kumar, L. Dubau, F. Maillard, G. Dražić, F. Jaouen, Identification of durable and non-durable FeN_x sites in Fe–N–C materials for proton exchange membrane fuel cells, *Nat. Catal.* 4 (2021) 10–19.
- [42] Y. He, Q. Shi, W. Shan, X. Li, A.J. Kropf, E.C. Wegener, J. Wright, S. Karakalos, D. Su, D.A. Cullen, G. Wang, D.J. Myers, G. Wu, Dynamically unveiling metal–nitrogen coordination during thermal activation to design high-efficient atomically dispersed CoN₄ active sites, *Angew. Chem. Int. Ed.* 60 (2021) 9516–9526.
- [43] L. Hu, C. Dai, L. Chen, Y. Zhu, Y. Hao, Q. Zhang, L. Gu, X. Feng, S. Yuan, L. Wang, B. Wang, Metal-triazolate-framework-derived FeN₄Cl₁ single-atom catalysts with hierarchical porosity for the oxygen reduction reaction, *Angew. Chem. Int. Ed.* 60 (2021) 27324–27329.
- [44] G. Chen, P. Liu, Z. Liao, F. Sun, Y. He, H. Zhong, T. Zhang, E. Zschech, M. Chen, G. Wu, J. Zhang, X. Feng, Zinc-mediated template synthesis of Fe–N–C electrocatalysts with densely accessible Fe–N_x active sites for efficient oxygen reduction, *Adv. Mater.* 32 (2020) 1907399.
- [45] Z. Chen, X. Liao, C. Sun, K. Zhao, D. Ye, J. Li, G. Wu, J. Fang, H. Zhao, J. Zhang, Enhanced performance of atomically dispersed dual-site Fe–Mn electrocatalysts through cascade reaction mechanism, *Appl. Catal. B Environ.* 288 (2021), 120021.
- [46] M. Liu, J. Lee, T.-C. Yang, F. Zheng, J. Zhao, C.-M. Yang, L.Y.S. Lee, Synergies of Fe single atoms and clusters on N-doped carbon electrocatalyst for pH-universal oxygen reduction, *Small, Methods* 5 (2021) 2001165.
- [47] Y. Zhou, Y. Yu, D. Ma, A.C. Foucher, L. Xiong, J. Zhang, E.A. Stach, Q. Yue, Y. Kang, Atomic Fe dispersed hierarchical mesoporous Fe–N–C nanostructures for an efficient oxygen reduction reaction, *ACS Catal.* 11 (2021) 74–81.
- [48] H. Yang, X. Chen, W.-T. Chen, Q. Wang, N.C. Cuello, A. Nafady, A.M. Al-Enizi, G.I. N. Waterhouse, G.A. Goenaga, T.A. Zawodzinski, P.E. Kruger, J.E. Clements, J. Zhang, H. Tian, S.G. Telfer, S. Ma, Tunable synthesis of hollow metal–nitrogen–carbon capsules for efficient oxygen reduction catalysis in proton exchange membrane fuel cells, *ACS Nano* 13 (2019) 8087–8098.
- [49] B. Li, S.P. Sasikala, D.H. Kim, J. Bak, I.-D. Kim, E. Cho, S.O. Kim, Fe–N₄ complex embedded free-standing carbon fabric catalysts for higher performance ORR both in alkaline & acidic media, *Nano Energy* 56 (2019) 524–530.
- [50] M. Wu, G. Zhang, J. Qiao, N. Chen, W. Chen, S. Sun, Ultra-long life rechargeable zinc-air battery based on high-performance trimetallic nitride and NCNT hybrid bifunctional electrocatalysts, *Nano Energy* 61 (2019) 86–95.
- [51] Y. Wu, Y. Wang, R. Wang, P. Zhang, X.-D. Yang, H. Yang, J.-T. Li, Y. Zhou, Z.-Y. Zhou, S.-G. Sun, 3D networks of S-doped Fe/N/C with hierarchical porosity for efficient oxygen reduction in polymer electrolyte membrane fuel cells, *ACS Appl. Mater. Interfaces* 10 (2018) 14602–14613.
- [52] L. Liu, G. Zeng, J. Chen, L. Bi, L. Dai, Z. Wen, N-doped porous carbon nanosheets as pH-universal ORR electrocatalyst in various fuel cell devices, *Nano Energy* 49 (2018) 393–402.
- [53] G. Zhu, Y. Qi, F. Liu, S. Ma, G. Xiang, F. Jin, Z. Liu, W. Wang, Reconstructing 1D Fe single-atom catalytic structure on 2D graphene film for high-efficiency oxygen reduction reaction, *ChemSusChem* 14 (2021) 866–875.
- [54] G.-S. Kang, J.-H. Jang, S.-Y. Son, C.-H. Lee, Y.-K. Lee, D.C. Lee, S.J. Yoo, S. Lee, H.-I. Joh, Fe-based non-noble metal catalysts with dual active sites of nanosized metal carbide and single-atomic species for oxygen reduction reaction, *J. Mater. Chem. A* 8 (2020) 22379–22388.
- [55] Y. Jiang, Y.-P. Deng, R. Liang, J. Fu, D. Luo, G. Liu, J. Li, Z. Zhang, Y. Hu, Z. Chen, Multidimensional ordered bifunctional air electrode enables flash reactants shuttling for high-energy flexible Zn-air batteries, *Adv. Energy Mater.* 9 (2019) 1900911.
- [56] T. Wang, X. Cao, H. Qin, L. Shang, S. Zheng, F. Fang, L. Jiao, P-block atomically dispersed antimony catalyst for highly efficient oxygen reduction reaction, *Angew. Chem. Int. Ed.* 60 (2021) 21237–21241.
- [57] L. Guan, F. Tan, G. Shen, Y. Liang, X. Xu, J. Guo, J. Wang, Z. Zhang, X. Li, Comparison of geometry models in the study of perovskite heterostructures, *Appl. Surf. Sci.* 475 (2019) 185–190.
- [58] F. Tian, D. Wang, F. Tan, X. Fang, W. Li, H. Wang, D. Wang, H. Zhao, D. Fang, Z. Wei, X. Wang, X. Ma, J. Li, Strain-dependent band structures and electronic

- properties in Sb/Bi lateral heterostructures calculated by first principles, *Phys. Status Solidi* 15 (2021) 2100148.
- [59] H.S. Kim, C.H. Lee, J.-H. Jang, M.S. Kang, H. Jin, K.-S. Lee, S.U. Lee, S.J. Yoo, W. C. Yoo, Single-atom oxygen reduction reaction electrocatalysts of Fe, Si, and N co-doped carbon with 3D interconnected mesoporosity, *J. Mater. Chem. A* 9 (2021) 4297–4309.
- [60] X. Wei, S. Song, N. Wu, X. Luo, L. Zheng, L. Jiao, H. Wang, Q. Fang, L. Hu, W. Gu, W. Song, C. Zhu, Synergistically enhanced single-atomic site Fe by Fe₃C@C for boosted oxygen reduction in neutral electrolyte, *Nano Energy* 84 (2021), 105840.